Supporting Information for:

On the Nature of Trapped-Hole States in CdS

Nanocrystals and the Mechanism of Their Diffusion

R. Peyton Cline, James K. Utterback, Steven E. Strong, Gordana Dukovic, and

Joel D. Eaves[*]

Department of Chemistry and Biochemistry, University of Colorado Boulder

Boulder, Colorado 80309-0215, United States

E-mail: Joel.Eaves@colorado.edu

_____

[*]To whom correspondence should be addressed

Contents

S.1 Derivation of the Diffusion Constants, $D_\parallel$ and $D_\perp$

We begin with a hole state located at site m as described in the main text. Here, we define this site m to be at the position (i, j), where i denotes the x-component and j denotes the y-component, and i and j take on discrete, integer values (Figure S1). In Figure S1, we define the crystal c-axis and orthorhombic x–y plane exactly as they are in the main text, with the crystal c-axis coinciding with the orthorhombic y-axis. We have rotated the lattice in the x–y plane clockwise by 90 degrees with respect to what is shown in the main text ("Top View" of Figure 1B, and Figure 4B) so that the x- and y-axis are now positioned in the typical fashion.

i-1, j+1   i, j+1   i+1, j+1

c-axis

i-1, j   i, j   i+1, j
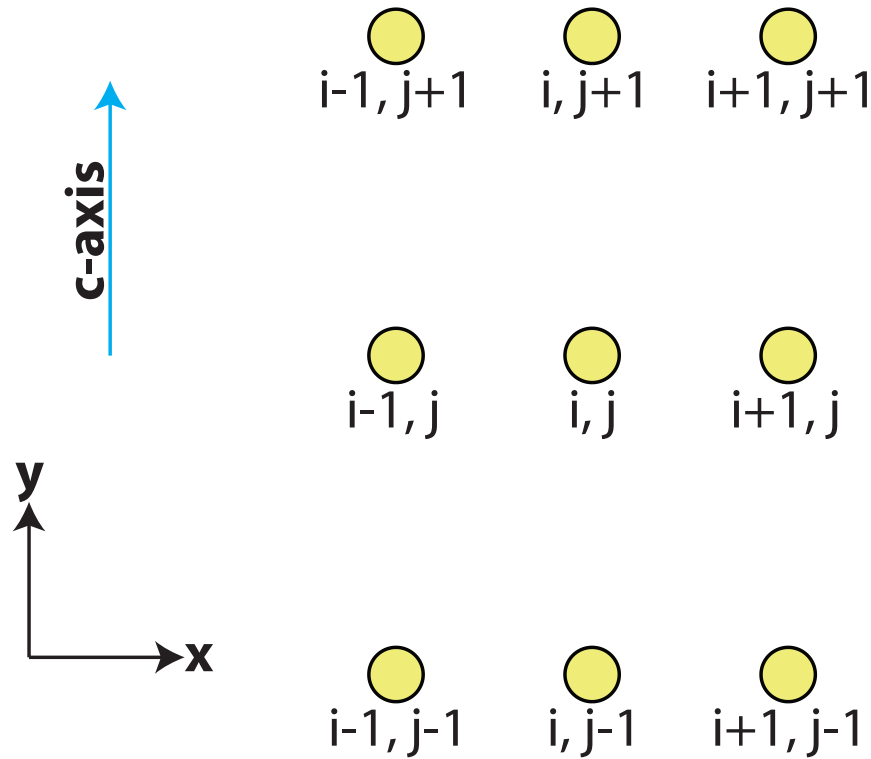
y

x

i-1, j-1   i, j-1   i+1, j-1

Figure S1: Schematic of the surface sulfur sites. A hole located at position (i, j) can jump to any of its nearest- and next-nearest-neighbors. Nearest-neighbors include $(i \pm 1, j)$ in the horizontal direction and $(i, j \pm 1)$ in the vertical direction. Next-nearest-neighbors include the remaining positions: $(i \pm 1, j \pm 1)$. The crystal c-axis and orthorhombic x–y plane are defined exactly as they are in the main text. We have rotated the lattice in the x–y plane clockwise by 90 degrees with respect to what is shown in the main text (Figure 1B and Figure 4B) so that the x- and y-axis are now positioned in the typical fashion (horizontal x, vertical y).

Utterback *et al.*[1] discovered that surface-trapped holes in CdS nanorods execute a diffusive random walk at room temperature. The equation governing the time evolution of a random walker starting at position $m = (i,j)$ and moving to any of its 8 nearest- or next-nearest-neighbors is

$$
\begin{aligned}
\frac{dP_{i,j}(t)}{dt} &= k_\perp \left[P_{i+1,j}(t) + P_{i-1,j}(t) - 2P_{i,j}(t) \right] \\
&+ k_\parallel \left[P_{i,j+1}(t) + P_{i,j-1}(t) - 2P_{i,j}(t) \right] \\
&+ k' \left[P_{i+1,j+1}(t) + P_{i-1,j-1}(t) - 2P_{i,j}(t) \right] \\
&+ k' \left[P_{i+1,j-1}(t) + P_{i-1,j+1}(t) - 2P_{i,j}(t) \right],
\end{aligned}
\tag{1}
$$

where $P_{i,j}(t)$ is the probability of finding a hole at position $m = (i,j)$ at time t; $k_\perp$, $k_\parallel$, and k' are the rates corresponding to the possible paths of motion (see Figure 4B in the main text). We define nearest-neighbors to be "on axis" in both dimensions at the positions $(i \pm 1, j)$ and $(i, j \pm 1)$, and we define next-nearest-neighbors to be "off axis" at positions $(i \pm 1, j \pm 1)$. In what follows, we derive the solution to eq 1 using approximation techniques and arrive at an anisotropic two-dimensional diffusion equation with two uncoupled diffusion constants, $D_\parallel$ and $D_\perp$. The approach we take here follows the derivation for one-dimensional diffusion presented in ref 2.

We first convert to a probability density $\mathcal{P}(x,y,t)$ by introducing an area, $dA = \alpha \varepsilon = \xi \varepsilon^2$, such that

$$
P_{i,j}(t) = \mathcal{P}(x,y,t)dA,
\tag{2}
$$

where x and y describe the positions i and j, respectively. The lengths, α and ε, correspond to the DFT-relaxed lattice spacings between sulfur atoms in the x- and y-directions, respectively, and their values are $\alpha = 4.2040$ Å and $\varepsilon = 6.8417$ Å. The quantity $\xi = \alpha/\varepsilon$ is a fixed aspect ratio of the lattice spacings on the rectangular lattice. We now convert eq 1 to a diffusion equation for the

probability density, $\mathcal{P}(x,y,t)$. Using the aspect ratio, ξ, to put all lengths in terms of ε, we find

$$
\begin{aligned}
\partial_t \mathcal{P}(x,y,t) = {} & k_\perp \Big[\mathcal{P}(x+\xi\varepsilon,y,t) + \mathcal{P}(x-\xi\varepsilon,y,t) - 2\mathcal{P}(x,y,t) \Big] \\
& + k_\| \Big[\mathcal{P}(x,y+\varepsilon,t) + \mathcal{P}(x,y-\varepsilon,t) - 2\mathcal{P}(x,y,t) \Big] \\
& + k' \Big[\mathcal{P}(x+\xi\varepsilon,y+\varepsilon,t) + \mathcal{P}(x-\xi\varepsilon,y-\varepsilon,t) - 2\mathcal{P}(x,y,t) \Big] \\
& + k' \Big[\mathcal{P}(x+\xi\varepsilon,y-\varepsilon,t) + \mathcal{P}(x-\xi\varepsilon,y+\varepsilon,t) - 2\mathcal{P}(x,y,t) \Big].
\end{aligned}
\tag{3}
$$

Our focus is to capture diffusion along the y-axis to compare with the results presented in ref 1; therefore, we want to expand each term in eq 3 asymptotically in ε. For any point (x,y), this yields

$$
\mathcal{P}(x,y,t) = \mathcal{P}^{(0)}(x,y,t) + \varepsilon \mathcal{P}^{(1)}(x,y,t) + \varepsilon^2 \mathcal{P}^{(2)}(x,y,t) + \ldots,
\tag{4}
$$

where the $\{\mathcal{P}^{(i)}\}$ are analytic functions. In the derivation to come, we only take eq 4 out to first order in ε for reasons that will soon become clear. Since the $\{\mathcal{P}^{(i)}\}$ are analytic functions in x and y, they also have Taylor series representations about points close to (x,y). For this derivation, we only need to take each Taylor expansion out to second-order; all odd-ordered terms cancel after substitution into eq 3. For compactness, we will temporarily suppress the time variable, t. Substituting eq 4 into eq 3 and Taylor expanding each relevant term to second-order, we find

$$
\begin{aligned}
\partial_t \mathcal{P}(x,y) \approx {} & \partial_t \Big[\mathcal{P}^{(0)}(x,y) + \varepsilon \mathcal{P}^{(1)}(x,y) \Big] \\
\approx {} & k_\perp \Big[\xi^2 \varepsilon^2 \partial_x^2 \mathcal{P}^{(0)}(x,y) + \varepsilon \big(\xi^2 \varepsilon^2 \partial_x^2 \mathcal{P}^{(1)}(x,y) \big) \Big] \\
& + k_\| \Big[\varepsilon^2 \partial_y^2 \mathcal{P}^{(0)}(x,y) + \varepsilon \big(\varepsilon^2 \partial_y^2 \mathcal{P}^{(1)}(x,y) \big) \Big] \\
& + k' \Big[2\xi^2 \varepsilon^2 \partial_x^2 \mathcal{P}^{(0)}(x,y) + 2\varepsilon^2 \partial_y^2 \mathcal{P}^{(0)}(x,y) + \varepsilon \big(2\xi^2 \varepsilon^2 \partial_x^2 \mathcal{P}^{(1)}(x,y) + 2\varepsilon^2 \partial_y^2 \mathcal{P}^{(1)}(x,y) \big) \Big].
\end{aligned}
\tag{5}
$$

It is notable that the second-order cross terms from the Taylor expansions cancel due to the symmetry of the problem and do not appear in eq 5. Upon rescaling time^2 as $\tau = \varepsilon^2 t$ and collecting

like terms, we arrive at

$$\partial_\tau \mathcal{P}^{(0)}(x,y,\tau) \approx \left[k_\perp \xi^2 \partial_x^2 + k_\| \partial_y^2 + k' \left(2\xi^2 \partial_x^2 + 2\partial_y^2 \right) \right] \mathcal{P}^{(0)}(x,y,\tau) \tag{6}$$

$$\partial_\tau \mathcal{P}^{(1)}(x,y,\tau) \approx \left[k_\perp \xi^2 \partial_x^2 + k_\| \partial_y^2 + k' \left(2\xi^2 \partial_x^2 + 2\partial_y^2 \right) \right] \mathcal{P}^{(1)}(x,y,\tau). \tag{7}$$

The above expressions illustrate that $\mathcal{P}^{(0)}(x,y,\tau)$ and $\mathcal{P}^{(1)}(x,y,\tau)$ have the same form, with $\mathcal{P}^{(1)}(x,y,\tau)$ providing higher-order corrections to the full $\mathcal{P}(x,y,\tau)$. Therefore, to *lowest order* in ε, the distribution $\mathcal{P}^{(0)}(x,y,\tau)$ captures the relevant physics for diffusion on a rectangular lattice. Putting the unscaled time, t, back into eq 6, we arrive at the final two-dimensional diffusion equation,

$$\partial_t \mathcal{P}^{(0)}(x,y,t) = \left[k_\perp \alpha^2 \partial_x^2 + 2k' \alpha^2 \partial_x^2 + k_\| \varepsilon^2 \partial_y^2 + 2k' \varepsilon^2 \partial_y^2 \right] \mathcal{P}^{(0)}(x,y,t)$$
$$= \left[D_\perp \partial_x^2 + D_\| \partial_y^2 \right] \mathcal{P}^{(0)}(x,y,t), \tag{8}$$

which depends on two uncoupled diffusion constants:

$$D_\perp = \alpha^2 (k_\perp + 2k') \tag{9}$$

$$D_\| = \varepsilon^2 (k_\| + 2k'). \tag{10}$$

Here, $D_\perp$ governs diffusion around the waist of a nanorod, and $D_\|$ governs diffusion down the c-axis of a nanorod. Utterback *et al.*[1] observed trapped-hole diffusion along the c-axis of their CdS nanorods, and from their experimental data, they calculated an upper bound for the corresponding diffusion constant, $D_\|$. They did not put a bound on $D_\perp$, and such an estimate is currently unknown; therefore, the focus of this work is dedicated only to $D_\|$. Lastly, because the value of $D_\|$ depends on the lattice spacing between surface sulfur atoms in the crystal c-direction, we replace ε from eq 10 with the letter c in the main text, yielding the final reported equation,

$$D_\| = c^2 (k_\| + 2k'). \tag{11}$$

S.2   Crystal Structure / VASP Convergence Details

S.2.1   Bulk Cell Parameters

The CdS bulk unit cell comprises four atoms with the following fractional positions: $(0,0,0)$ and $(\frac{1}{3}, \frac{2}{3}, \frac{1}{2})$ for Cd; $(0,0,0.37715)$ and $(\frac{1}{3}, \frac{2}{3}, 0.87715)$ for S.[3] We define the corresponding unit cell with lattice parameters $a = 4.136$ and $c = 6.713$ and the vectors $(a,0,0)$, $(-\frac{a}{2}, \frac{a\sqrt{3}}{2}, 0)$, and $(0,0,c)$. These definitions yield a wurtzite crystal structure. Using these parameters, we construct a $2 \times 2 \times 2$ bulk supercell and a $3 \times 3 \times 4$ bulk supercell. We will discuss the reasons for the latter bulk cell in the coming sections (section S.2.4). We create all variants of surface "slab" supercells from these two bulk cells. All VASP (Vienna Ab initio Simulation Package) calculations presented are non spin-polarized, and we enforce a 520 eV plane-wave energy cutoff (1.9 times the default). All k-point meshes are centered at the Γ-point. All structural relaxations make use of the conjugate gradient algorithm.

S.2.2   Bulk Convergence Details

For the $2 \times 2 \times 2$ supercell, we use a $6 \times 6 \times 4$ k-point mesh, which converges the energy to less than 0.01 meV/atom relative to the most dense k-point mesh we considered, a $24 \times 24 \times 16$ mesh. We achieve similar convergence for the $3 \times 3 \times 4$ supercell by using a $4 \times 4 \times 2$ k-point mesh. We relax all degrees of freedom (ionic positions, cell volume, and cell shape) for each bulk supercell and employ the tetrahedron method with Blöchl corrections as the method of smearing. For bulk CdS, this method is variational since no partial occupancies appear in the band structure. We use an additional support grid for the evaluation of augmentation charges, in combination with "high" precision and an augmentation-charge cutoff energy of 520 eV, to reduce the noise in the forces. We find "high" precision works better than the more modern "accurate" precision by providing the smallest noise in forces for bulk CdS. Using these settings, we require strict cutoffs of 1×10^{-4} eV/Å for the force convergence and 1×10^{-9} eV for the energy convergence of each ionic step.

S.2.3 $(10\bar{1}0)$ Surface Slab Parameters

According to Sun and Ceder,[4] one can define the $(10\bar{1}0)$ Miller-Bravais facet of a hexagonal/wurtzite cell with a simple orthorhombic cell by performing a symmetry transform of the old hexagonal coordinates. Such a transformation is useful because defining a surface slab cell with completely orthorhombic coordinates minimizes k-point dispersion errors during a calculation.[4] Furthermore, this transformation makes band structure and density of states (DOS) calculations unambiguous in terms of k-point sampling. Indeed, previous work by Rantala *et al.*[5] defined a CdS $(10\bar{1}0)$ surface with an orthorhombic cell. Using the code presented by Sun and Ceder,[4] we successfully transform the coordinates of the DFT-relaxed bulk supercells to orthorhombic coordinates, and with the z-axis perpendicular to the $(10\bar{1}0)$ facet. Here and in the main text, we refer to the dimensions of the surface slabs using the new orthorhombic x–y–z coordinates instead of the original wurtzite a–b–c coordinates. The various surface slab sizes we consider are as follows:

- two $2 \times 2 \times 8$ surfaces (symmetric and asymmetric),

- one $2 \times 2 \times 3$ surface (asymmetric),

- one $3 \times 4 \times 3$ surface (asymmetric),

where the symmetric and asymmetric labels correspond to the passivation/relaxation scheme we employ (see section S.2.5).

We vary the thickness and relaxation scheme between slabs to test for convergence of the surface geometry, which is important for achieving convergence of the tunneling matrix elements (results in Table S1). We only report on the $2 \times 2 \times 8$ symmetric surface slab in the main text. As evident from the dimensionalities, we construct all $2 \times 2 \times N$ surface slabs from the DFT-relaxed $2 \times 2 \times 2$ bulk supercell, and we construct the thin, wide $3 \times 4 \times 3$ surface slab from the DFT-relaxed $3 \times 3 \times 4$ bulk supercell. The mismatch of the indices between the $3 \times 4 \times 3$ surface slab and the $3 \times 3 \times 4$ bulk supercell arises from the change to orthorhombic coordinates, where the wurtzite c-axis (third index for the bulk supercell) coincides with the orthorhombic y-axis (second index for the surface slab).

S.2.4 $3 \times 4 \times 3$ "Anti-Aliased" Surface Slab

The purpose of constructing a wide $3 \times 4 \times 3$ surface slab (3×4 surface, 3 layers in thickness) is to determine if wave function aliasing is an issue for the Wannier localization procedure. We use a $3 \times 4 \times 3$ slab instead of a $3 \times 3 \times 3$ slab because pseudohydrogen passivation (see section S.2.5) introduces fractional electrons per individual species, and a $3 \times 4 \times 3$ slab guarantees that the total electron count is a whole number. The concern for the wave function aliasing effect is that the distances between nearest-neighbor sulfur atoms on the surface are roughly $L/2$ apart in the $2 \times 2 \times N$ slabs, where L is the length of the slab cell in either the x- or y-direction. This $L/2$ separation is the greatest distance two neighboring surface sulfur atoms can be from each other in the $2 \times 2 \times N$ periodic system, suggesting that unphysical interactions with their periodic images may occur. Because of this, one could conclude that the periodic copies of the electron density calculated by VASP lead to unphysical delocalization of the final diabatic states. This would lead to artificially high values of the tunneling matrix elements presented in the main text, thereby implying diffusion is "fast" relative to the actual value. Our findings for the $3 \times 4 \times 3$ surface slab, located in Table S1, suggest that wave function aliasing is not an issue since the calculated tunneling matrix elements are nearly identical to those of the $2 \times 2 \times 3$ slab, which was relaxed using comparable settings (see Table S1).

S.2.5 Pseudohydrogen Passivation and Ionic Relaxation Scheme

For all surface slabs, we begin by capping all surface cadmium and sulfur atoms with their respective pseudohydrogen (PH) species. We relax the positions of the PH atoms until the forces they experience fall below 10 meV/Å to ensure proper passivation and to ensure all slabs start from similar initial conditions. From here, we construct the symmetric and asymmetric cases as follows. For the symmetric $2 \times 2 \times 8$ case (Figure S2A), we uncap all sulfur atoms on both surfaces, leaving only the surface cadmium atoms passivated. We hold the middle 2 layers of CdS fixed at their initial positions and relax all other atoms in a "middle-out" manner, thereby simulating surface-like behavior at both ends. For all asymmetric surface variants (Figure S2B), we keep full passivation
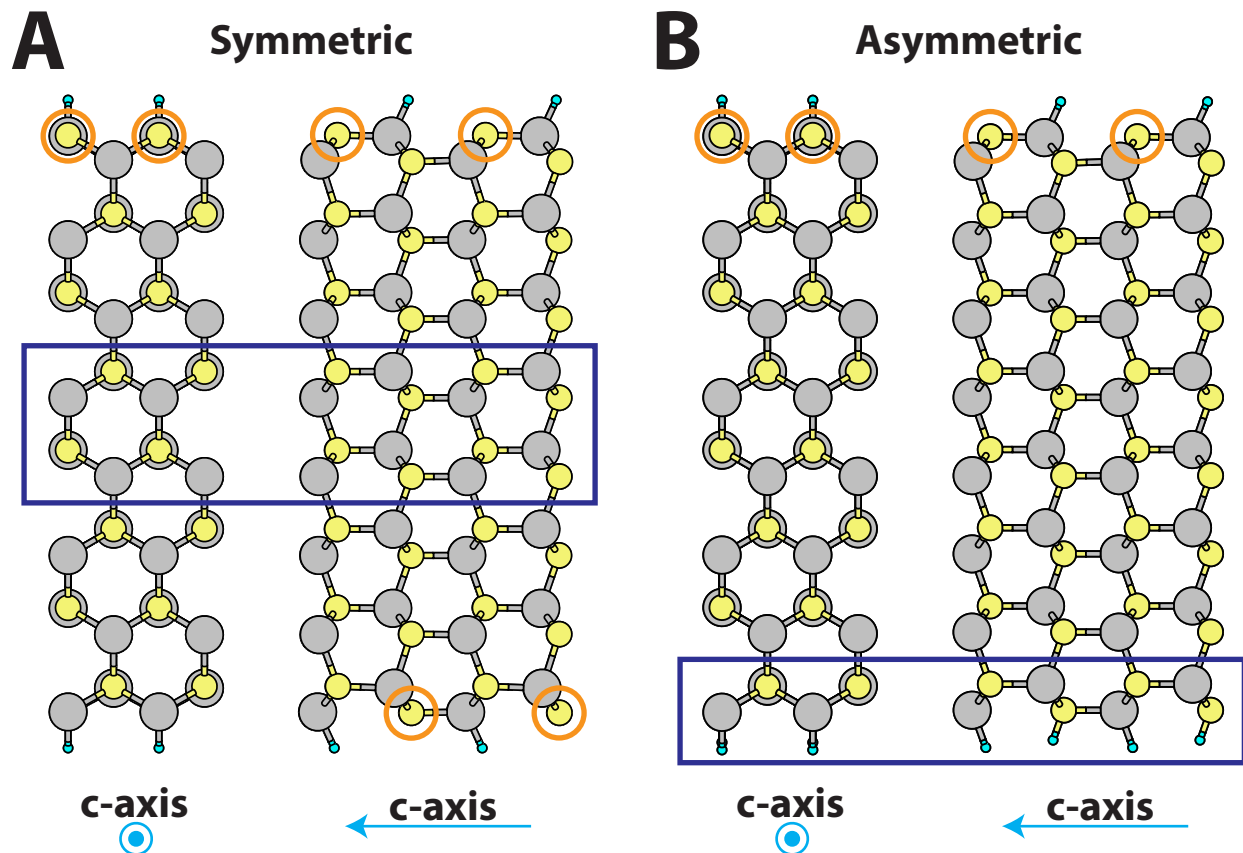
Figure S2: Side views of $2 \times 2 \times 8$ symmetric and asymmetric surface slabs. Cadmium atoms are gray, sulfur atoms are yellow, and pseudohydrogen (PH) passivants are blue. Surface sulfur atoms are labeled with orange circles. The regions boxed in dark blue contain the fixed, "bulk-like" atoms. (A) The symmetric slab. Only the surface cadmium atoms are passivated in the slab, leaving all surface sulfur atoms undercoordinated by 1 bond. The boxed region contains 2 layers of CdS. (B) The asymmetric slab. PH atoms passivate all cadmium and sulfur atoms on the bottom surface. Cadmium atoms on the top surface are also passivated, while sulfur atoms on the top surface are undercoordinated by 1 bond. The boxed region contains 1 layer of PH atoms and 1 layer of CdS. The thinner asymmetric slabs (not shown) follow the same passivation scheme as the $2 \times 2 \times 8$ asymmetric slab.

on the bottom surface to completely eliminate surface states arising from that layer. On the top surface, we remove all sulfur-capped PH species and leave the cadmium passivation intact, thus simulating the presence of hole states on the top surface only. We enforce that the bottom layer of PH and the adjacent layer of CdS represent the "bulk-like" part of the system during relaxation by keeping their positions fixed at all times. We allow all other atoms to relax. We do not charge the system or account for differences in geometry between the uncharged and charged systems for any

calculation. Thus, we employ the Condon and frozen orbital approximations for all calculations.

S.2.6 Surface Convergence Details

For the slab calculations, we turn symmetrization protocols off except for $|\Psi_\mathbf{k}\rangle = |\Psi_{-\mathbf{k}}\rangle$, where $|\Psi_\mathbf{k}\rangle$ is the Bloch state at wave vector $\mathbf{k}$. During relaxations, we require a force convergence cutoff of 10 meV/Å and an energy convergence cutoff of 1×10^{-6} eV for each ionic step. We employ Gaussian smearing during geometry relaxations, keeping the cell shape and volume fixed. The tetrahedron method is not viable for our surface slab relaxations because of partial occupancies in the band structure that arise from the undercoordinated sulfur atoms at the surface. We again use an additional support grid for the evaluation of augmentation charges. For all calculations except the $2 \times 2 \times 8$ surfaces, we use "accurate" precision because this minimizes the noises in the forces. For the $2 \times 2 \times 8$ variants, however, we find the "high" precision tag with an augmentation-charge cutoff energy of 750 eV provides the best accuracy in the forces.

Keeping the previous settings fixed, we carry out numerous convergence tests for the tunneling matrix elements, $t_\perp$, $t_\parallel$, and t', using the slabs mentioned in section S.2.3. To test for convergence for each slab, we vary the k-point density and the smearing width since partial occupancies arise in the band structure near the Fermi energy, E_F. These partial occupancies require that we carefully sample the Brillouin zone to achieve the most accurate ground-state surface geometry. The results, summarized in Table S1, show that the matrix elements are fairly insensitive to the k-point mesh and smearing width choices we considered, implying that our lowest-quality choices are adequate for finding the approximate ground-state surface structure. This is especially evident in the results for the symmetric $2 \times 2 \times 8$ slab, where all variants yield $|t_\parallel| \approx |t'| \approx 3$ meV and $|t_\perp| \approx 80$ meV. The calculated lower bound on the reorganization energy, $\lambda \geq 1$ eV, is the same for all calculations presented in Table S1. We use 293 K as the definition for room temperature when calculating λ.

Table S1: Calculated tunneling matrix elements for the surface slabs. We test convergence of the matrix elements by employing various k-point meshes and Gaussian smearing widths during structural relaxations. The (s) and (a) labels for the $2 \times 2 \times 8$ surfaces denote symmetric and asymmetric, respectively. All other surfaces are asymmetric by default.

surface	k-point mesh	smearing (meV)	$|t_\perp|$ (meV)	$|t_\parallel|$ (meV)	$|t'|$ (meV)
$2 \times 2 \times 3$	$6 \times 4 \times 1$	50	79.1	2.2	3.6
	$8 \times 5 \times 1$	2	79.1	2.5	3.4
	$12 \times 8 \times 1$	2	79.1	2.5	3.4
$2 \times 2 \times 8(s)$	$6 \times 4 \times 1$	50	80.0	3.0	2.9
	$8 \times 5 \times 1$	10	79.8	2.9	3.0
	$8 \times 5 \times 1$	2	79.8	2.9	3.0
$2 \times 2 \times 8(a)$	$6 \times 4 \times 1$	50	79.8	2.9	2.9
	$8 \times 5 \times 1$	2	79.6	3.2	2.8
$3 \times 4 \times 3$	$4 \times 2 \times 1$	50	79.4	2.2	3.6

S.3   Wannier Localization Procedure

S.3.1   Wannier90: A Brief Description

Wannier90 converts the adiabatic plane-wave results to maximally-localized Wannier functions (MLWFs) through a series of unitary transformations of the original Bloch states. Wannier90 quantifies the degree of localization by calculating the spatial "spread" of the orbitals, which the code minimizes to generate the MLWFs. The spread takes on units of Å^2. Details and additional information on these topics can be found in the Wannier90 manual and various references.[6–9]

S.3.2   Convergence Criteria

For our system and choice of MLWF basis (sulfur-centered sp^3 orbitals), Wannier90 must complete two phases: "disentanglement" and "Wannierisation." The former extracts the optimal subspace of states from the original DFT calculation for building the MLWFs, and the latter maximally localizes these states. For all calculations, we use the default disentanglement convergence criteria supplied by Wannier90: disentanglement terminates when the fractional change between successive iterations in the spread is less than 1×10^{-10} Å^2 for 3 iterations. For the Wannierisation phase, we enforce a convergence of 1×10^{-11} Å^2 over 10 successive iterations for the fractional

change in the spread. We find that convergence is most stable when we construct sulfur-centered sp^3 orbitals throughout the entire structure. In fact, doing so leads directly to the first tight-binding Hamiltonian, $\mathcal{H}_{TB}$, discussed in the main text.

S.3.3 The Outer and Inner Energy Windows

The two most important tunable parameters that determine how the spread is minimized are the "outer" and "inner" energy windows. The outer window should encompass any states believed to contribute to the desired diabatic picture, and the inner window should encompass only the states that need to be reproduced exactly after Wannier localization. The inner window is often called the "frozen" window for this reason. For all calculations, we set the outer window to include all states below $E_F + 0.2$ eV. This choice excludes all purely-unoccupied (conduction) bands that exist above $E_F + 1.3$ eV since we find that the conduction bands do not aid in constructing the sp^3 orbital subspace.

Determining the inner window range is a much more delicate process that requires extensive testing since the choice of inner window may dramatically alter some of the desired properties. Because the hole states localized on surface sulfur atoms correspond to the top-most bands of the valence manifold, we know that we need to preserve, *at a minimum*, the electronic properties of the region between E_F and $E_F + 0.2$ eV. Therefore, we set the initial inner window to encompass the states in this region. Since we define the inner window maximum to coincide with the outer window maximum, this value need not change if we must preserve all states between E_F and $E_F + 0.2$ eV. Thus, the inner window minimum, which has an upper bound equal to E_F, is the only unknown variable we still need to determine for our system.

In the main text, we show that the hole states are well localized on the surface sulfur atoms; therefore, we use the spread of the converged nonbonding sp^3 orbitals in the system to determine the proper inner window minimum value for all calculations. We use this as a metric for the following reason: increasing the width of the inner window for a fixed outer window range will always increase the *total* spread since the inner window imposes a constraint on the final diabatic

states; however, *individual* spreads need not follow this trend. As such, we hypothesize that some value of the inner window minimum will minimize the spreads of the nonbonding sp^3 orbitals within the manifold of all sulfur-centered sp^3 orbitals. Taking into account this information, we perform numerous Wannier localizations for all slabs starting with an inner window minimum value of E_F and scanning below to the nearest meV to determine the optimal value. For this work, an inner window width of about 1.6 eV, corresponding to an inner window minimum value of approximately $E_F - 1.4$ eV, leads to maximally-localized nonbonding sp^3 orbitals for all $2 \times 2 \times 8$ slabs. For the symmetric $2 \times 2 \times 8$ slab in particular, the nonbonding sp^3 orbitals attain final spreads of $\sim$1.6 Å^2, and all sp^3 orbitals in the structure in general attain spreads between 1.6 and 2.1 Å^2.

S.4 Alternate Electronic Structure Comparisons

S.4.1 Fully-Passivated $2 \times 2 \times 8$ Surface Slab

In the main text, we mention that passivating all surface sulfur and cadmium atoms with their respective PH species gives rise to "bulk-like" behavior. Figure S3A shows a DOS calculation for such a fully-passivated surface slab, which we construct by taking our final $2 \times 2 \times 8$ symmetric slab (10 meV smearing width, Table S1) and then passivating the bare sulfur atoms. We relax the positions of these PH species, holding all other atoms fixed, to ensure complete passivation of the surface sulfur dangling bonds. In this DOS, we notice no states exist immediately above the "Fermi" level, E_F, which here is defined as the energy at the valence band maximum. *All* states below E_F are fully occupied and *all* states above E_F are completely unoccupied; no partial occupancies exist with this passivation scheme. To compare with bulk CdS, we calculate the DOS for the relaxed $2 \times 2 \times 2$ bulk supercell, shown in Figure S3B. As evident, there is qualitatively no difference in the DOS between the fully-passivated surface slab and a bulk cell. We verify these results by inspecting the electron density for the surface slab within 25 meV below E_F. The results (Figure S3C) show that all of the electron density in this energy range resides in the bulk of the material, *delocalized* throughout most of the structure, with no discernible states localized to the
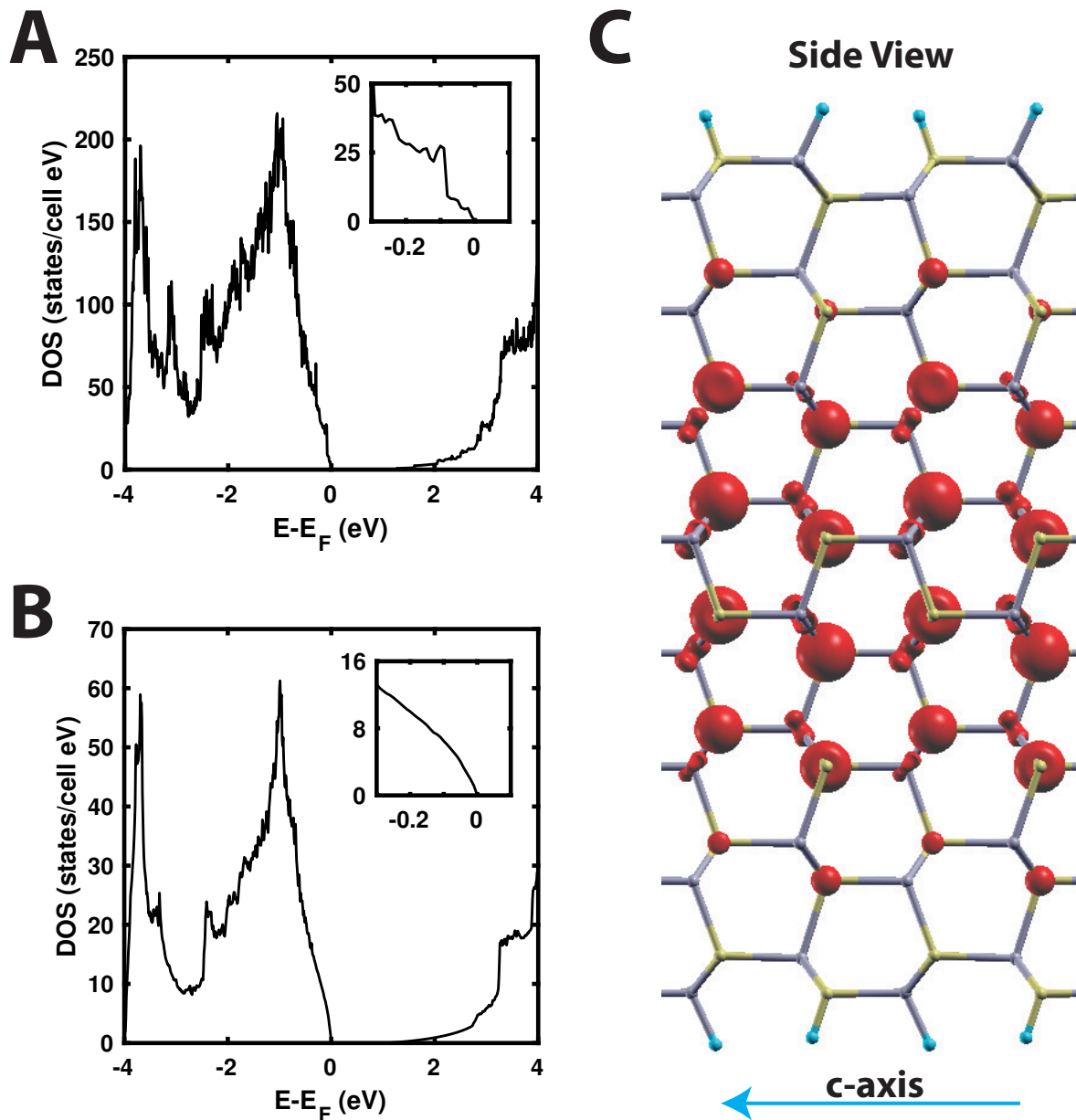
surface sulfur atoms.

Figure S3: (A) Total DOS within the range $E_F \pm 4$ eV for a fully-passivated $2 \times 2 \times 8$ surface slab, showing the elimination of states beyond E_F. (B) Total DOS within the range $E_F \pm 4$ eV for the $2 \times 2 \times 2$ bulk supercell. Qualitatively, there is virtually no difference between the two DOS calculations. (C) Fully-passivated $2 \times 2 \times 8$ surface slab electron density (red) at the valence maximum (between the range $E_F - 0.025$ eV and E_F).

S.4.2 Asymmetric $2 \times 2 \times 8$ Surface Slab

Here, we compare the calculations presented in the main text for the converged $2 \times 2 \times 8$ symmetric slab to those of a $2 \times 2 \times 8$ asymmetric slab, whose final positions were calculated using an $8 \times 5 \times 1$ k-point mesh and a smearing width of 2 meV. The results for the DOS (Figure S4A) reveal that the asymmetric and symmetric variants yield qualitatively the same DOS, with a region between E_F and $E_F + 0.2$ eV containing bands that are mostly unoccupied. E_F here is exactly as it is in the main text: the energetic point at which bands are exactly 50% occupied. An electron density calculation of the states between E_F and $E_F + 0.2$ eV for the asymmetric slab gives the same result as seen in the main text, so we do not show that result here for the asymmetric slab. Figure S4B shows the corresponding band structure for the $2 \times 2 \times 8$ asymmetric slab. Like with the DOS, we find qualitative agreement between this band structure and the one found in the main text (Figure 3) for the symmetric slab.
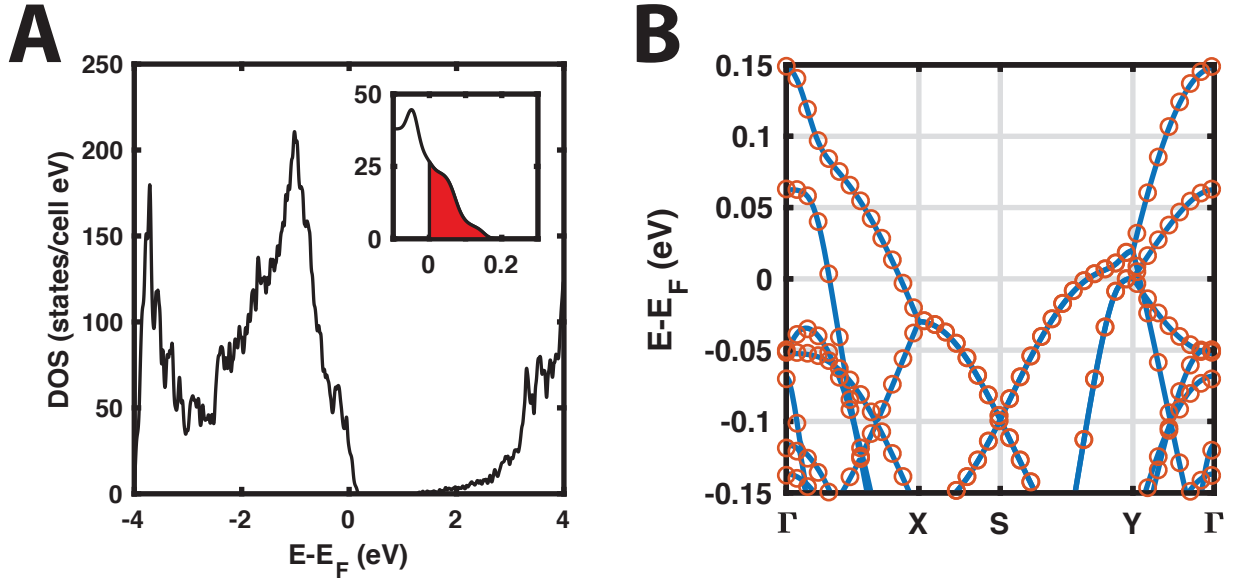

Figure S4: (A) Total DOS within the range $E_F \pm 4$ eV for the $2 \times 2 \times 8$ asymmetric slab relaxed using an $8 \times 5 \times 1$ k-point mesh. We see qualitatively similar results as those described in the main text. (B) Band structure calculation for the $2 \times 2 \times 8$ asymmetric slab. Again, we find qualitatively similar results with those found in the main text.

References

(1) Utterback, J. K.; Grennell, A. N.; Wilker, M. B.; Pearce, O. M.; Eaves, J. D.; Dukovic, G. Observation of Trapped-Hole Diffusion on the Surfaces of CdS Nanorods. *Nat. Chem.* **2016**, *8*, 1061–1066.

(2) Van Kampen, N. G. *Stochastic Processes in Physics and Chemistry*, 3rd ed.; Elsevier: Amsterdam, The Netherlands, 2007.

(3) Ekuma, E. C.; Franklin, L.; Zhao, G. L.; Wang, J. T.; Bagayoko, D. Local Density Approximation Description of Electronic Properties of Wurtzite Cadmium Sulfide (w-CdS). *Can. J. Phys.* **2011**, *89*, 319–324.

(4) Sun, W.; Ceder, G. Efficient Creation and Convergence of Surface Slabs. *Surf. Sci.* **2013**, *617*, 53–59.

(5) Rantala, T. T.; Rantala, T. S.; Lantto, V.; Vaara, J. Surface Relaxation of the ($10\bar{1}0$) Face of Wurtzite CdS. *Surf. Sci.* **1996**, *352*, 77–82.

(6) Marzari, N.; Vanderbilt, D. Maximally Localized Generalized Wannier Functions for Composite Energy Bands. *Phys. Rev. B: Condens. Matter Mater. Phys.* **1997**, *56*, 12847–12865.

(7) Souza, I.; Marzari, N.; Vanderbilt, D. Maximally Localized Wannier Functions for Entangled Energy Bands. *Phys. Rev. B: Condens. Matter Mater. Phys.* **2001**, *65*, 035109.

(8) Mostofi, A. A.; Yates, J. R.; Lee, Y.-S.; Souza, I.; Vanderbilt, D.; Marzari, N. Wannier90: A Tool for Obtaining Maximally-Localised Wannier Functions. *Comput. Phys. Commun.* **2008**, *178*, 685–699.

(9) Marzari, N.; Mostofi, A. A.; Yates, J. R.; Souza, I.; Vanderbilt, D. Maximally Localized Wannier Functions: Theory and Applications. *Rev. Mod. Phys.* **2012**, *84*, 1419–1475.